



# Characteristics of Crack-Free Silicon Nitride Films Deposited by LPCVD for Photonic Applications

Donghao Li<sup>1,2</sup> · Bin Li<sup>1</sup> · Bo Tang<sup>1</sup> · Peng Zhang<sup>1</sup> · Yan Yang<sup>1</sup> · Ruonan Liu<sup>1</sup> · Ling Xie<sup>1</sup> · Zhihua Li<sup>1</sup>

Received: 6 June 2021 / Accepted: 27 August 2021 / Published online: 29 September 2021  
© The Minerals, Metals & Materials Society 2021

## Abstract

Silicon photonics has emerged as one of the most prominent technological platforms for photonic integration. Compared with silicon, silicon nitride has a much broader wavelength transparency range, lower propagation loss, and less sensitivity to temperature changes, making it suitable for the manufacture of passive devices. However, silicon nitride films deposited directly on the wafer by low-pressure chemical vapor deposition exhibit large tensile stress, which may cause cracks. In the work presented herein, a process was developed to fabricate crack-free 400-nm-thick silicon nitride films based on the 200-mm complementary metal–oxide–semiconductor platform. The silicon nitride films were deposited in two steps, each followed by annealing. During the annealing, Si–H and N–H bonds in the film were broken and Si–N bonds were formed, thus improving the uniformity of the film and releasing the stress. Fourier-transform infrared measurements indicated that the films were in near-stoichiometric condition. Wafer-level testing showed that the propagation loss of an 800-nm-wide strip waveguide was 0.5 dB/cm to 0.7 dB/cm for the C-band. The insertion loss of waveguide crossing was approximately 0.15 dB, and the crosstalk was below –43 dB. The insertion loss of 1 × 2 multimode interference was less than 0.3 dB, and the nonuniformity was smaller than 10%.

**Keywords** Silicon nitride · LPCVD · annealing · low stress · wafer-level test · waveguide

## Introduction

Silicon photonics provides a key technological platform that paves the way for large-scale photonic integration, featuring low cost and compatibility with complementary metal-oxide–semiconductor (CMOS) processes.<sup>1,2</sup> This has led to its widespread application in several domains such as high-speed optical transceivers, laser radar, sensing, quantum computing, and neuromorphic networks.<sup>3–8</sup> However, some of the intrinsic properties of silicon pose challenges to the performance of devices in these applications; For instance, although conducive for the realization of optical switching, the high thermo-optical coefficient of silicon

makes silicon-on-insulator (SOI) devices strongly sensitive to temperature variations. In addition, the existence of two-photon absorption makes SOI devices potentially inefficient in applications with high power density or for all-optical processing.<sup>9</sup> Compared with silicon, silicon nitride and silicon dioxide have lower index contrast and higher mode limitation in waveguides, which relaxes the fabrication tolerance and reduces the sidewall roughness scattering. The bandgap of silicon nitride is about 5.0 eV, making it transparent in the wavelength range from visible to mid-infrared.<sup>10</sup> Furthermore, the thermo-optical coefficient of silicon nitride is one order of magnitude smaller than that of silicon, so silicon nitride devices can maintain stable performance at various temperatures. Finally, silicon nitride exhibits negligible two-photon absorption at a wavelength of 1550 nm.<sup>11</sup> All these properties make silicon nitride an ideal material for use in passive photonic devices.

Silicon nitride films are usually deposited by low-pressure chemical vapor deposition (LPCVD) at high temperature (> 800°C) or plasma-enhanced chemical vapor deposition (PECVD) at low temperature (< 400°C).<sup>12</sup> In fact, the composition of such films tends to deviate from

✉ Bin Li  
libin1@ime.ac.cn

✉ Zhihua Li  
lizhihua@ime.ac.cn

<sup>1</sup> Institute of Microelectronics, Chinese Academy of Sciences, Beijing, China

<sup>2</sup> School of Microelectronics, University of Chinese Academy of Sciences, Beijing, China

stoichiometric  $\text{Si}_3\text{N}_4$  due to the formation of N–H bonds during the deposition process.<sup>13,14</sup> N–H bonds exhibit a strong absorption peak near a wavelength of 1520 nm,<sup>15</sup> which increases the propagation loss of the waveguide. Deposition of silicon nitride films by LPCVD at high temperatures provides sufficient energy to break the N–H bonds, making them more suitable for the manufacture of low-loss photonic devices. However, LPCVD-based silicon nitride films that are deposited directly on the wafer show high tensile stress, and the wafer will crack if the stress exceeds the strength of the silicon nitride films.<sup>16</sup>

In the work presented herein, high-quality 400-nm-thick silicon nitride films were obtained on the 200-mm CMOS platform through LPCVD and annealing in two steps, which can effectively solve the problem of stress in the deposition process. The whole fabrication process of the silicon nitride films is first described. Then, the properties of the silicon nitride films and the performance of wafer-level optical passive devices are discussed.

### Experimental Procedures

The whole process for forming 400-nm-thick silicon nitride films was carried out on the 200-mm CMOS platform, as shown in Fig. 1. The fabrication started with 3- $\mu\text{m}$ -thick thermal oxidation of the silicon substrate.

#### Deposition of Silicon Nitride Films

Silicon nitride films were deposited by LPCVD in two steps to reduce the stress. With the increase of the mean free path of gas molecules, the diffusion rate of molecules is accelerated at low pressure, thus improving the deposition rate of films.<sup>17</sup> At the same time, at low pressure, gas molecules have less chance of collision in the transport process, so there is less possibility of generating contaminants on the film surface. As a result, LPCVD-based silicon nitride films have less particle pollution and high uniformity of thickness.

To obtain 400-nm-thick films, the first deposition thickness was 250 nm and the second deposition thickness was 200 nm, because subsequent processing, such as annealing

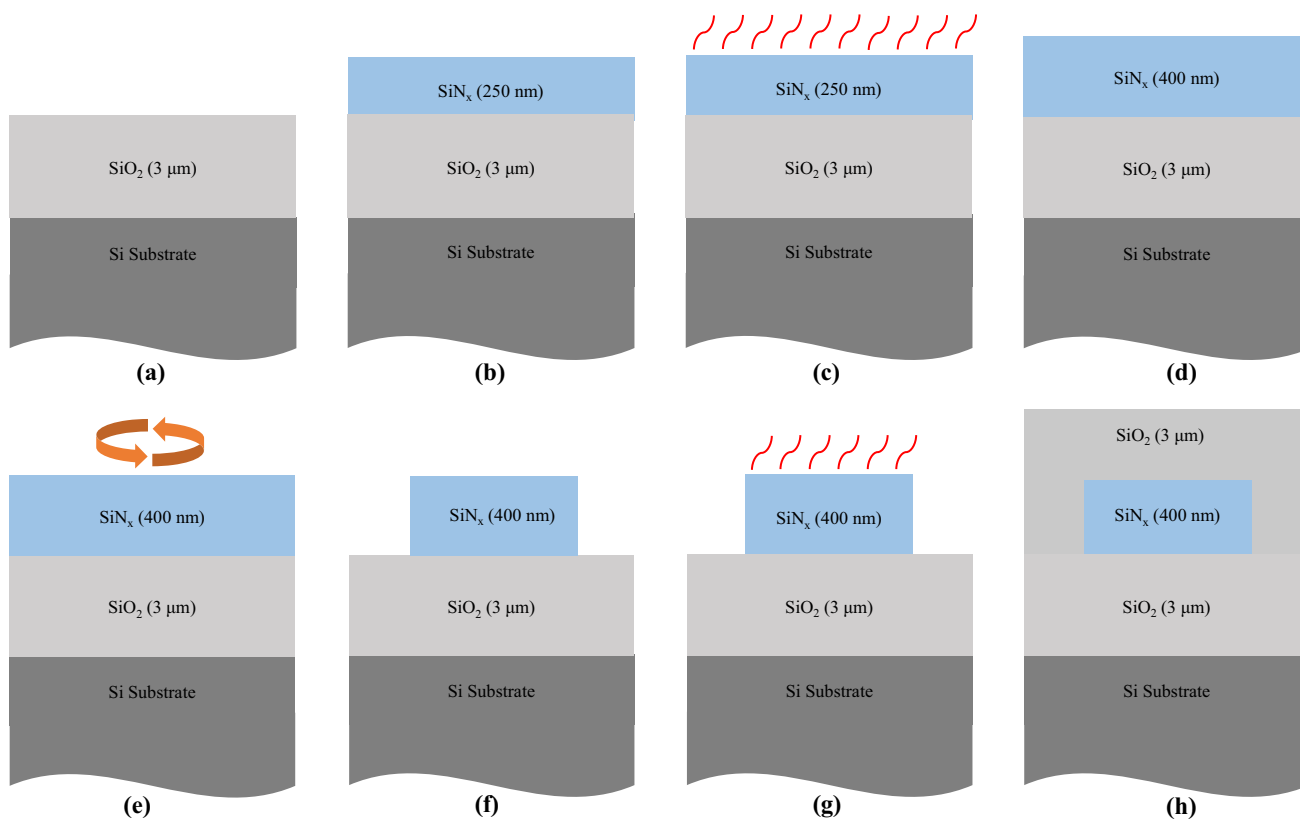


**Fig. 1** Cross-section of 400-nm-thick silicon nitride films process flow: (a) 3- $\mu\text{m}$ -thick thermal oxidation of the silicon substrate, (b) first deposition of 250-nm silicon nitride films by LPCVD, (c) annealing at 1050°C for 9 h and chemical–mechanical polish-

ing (CMP), (d) second deposition of 200-nm silicon nitride films by LPCVD, (e) CMP, (f) lithography and etching, (g) annealing at 1050°C for 9 h, and (h) deposition of 3- $\mu\text{m}$ -thick silicon dioxide as upper cladding

and chemical–mechanical polishing (CMP), would make the films thinner. The films were deposited in an Applied Materials Centura SiNgen single-wafer reactor with  $\text{SiH}_4/\text{NH}_3/\text{N}_2$  as source gases under  $3.67 \times 10^{-2}$  kPa pressure at  $800^\circ\text{C}$ . During the second deposition, the wafer was rotated by  $45^\circ$  in order to distribute the uniaxial strain through the overall film thickness and reduce the accumulation of tensile stress.<sup>16</sup> After deposition of the silicon nitride films, CMP was used to reduce the surface roughness, which is beneficial to reduce light scattering from the surface and grain boundaries.<sup>18</sup> The surface roughness of the silicon nitride films was investigated by atomic force microscopy (DIMENSION ICON) over an area of  $5 \mu\text{m} \times 5 \mu\text{m}$ ; the results are shown in Fig. 2. The root-mean-square roughness ( $R_q$ ) of the surface was about 0.036 nm.

### Hyperthermal Annealing

During hyperthermal annealing, Si–H and N–H bonds in the film are broken and Si–N bonds are formed, releasing H atoms, which makes the films more compact and thinner. Due to the film densification and viscous flow, the residual stress in the silicon nitride films increased at the early stage of annealing and then decreased in the subsequent annealing process.<sup>19</sup> The silicon nitride films were annealed at  $1050^\circ\text{C}$  for 9 h in  $\text{N}_2$  atmosphere. The first annealing process was carried out after the first deposition of silicon nitride films, while the second annealing was carried out after lithography and etching. This is because etching can release some stress to prevent the films from cracking at the early stage of annealing.

### Lithography and Etching

During the lithography process, 800-nm-thick photoresist was used for spin coating. Deep-ultraviolet (DUV)

lithography was used to define the waveguide and device patterns on the photoresist as a soft mask. An inductively coupled plasma (ICP) etching process was utilized to transfer the patterns from the photoresist layer to the silicon nitride films.  $\text{CF}_4$  and  $\text{CHF}_3$  were used as etching gas under  $4.26 \times 10^{-3}$  kPa pressure, and the  $\text{SiO}_2$  buried oxide was used as an etch-stop layer. The etching selectivity of the photoresist against the nitride layer was about 1:1. Scanning electron microscopy (SEM) of waveguides was used to analyze the etching morphology (Fig. 3). The actual width of the waveguide obtained by etching was 808 nm (versus a designed width of 800 nm), and the sidewall inclination was about  $85.5^\circ$ , which satisfies the requirements for photonic devices.

## Results and Discussion

### Film Analysis

#### Thickness Analysis

A thin-film thickness measurement system (Nanometrics Nanospec 9100) was used to measure the thickness of the silicon nitride films. Figure 4a, b shows representative thickness maps of silicon nitride films deposited by LPCVD. It can be seen that the film thickness after the first deposition was uniform, with an average of 249.5 nm and a standard deviation of 4.90 nm ( $< 2\%$ ). The uniformity of the films was worse after the second deposition, because the process parameters were adjusted to reduce the stress during the second deposition.

The final thickness of the films was about 385 nm, which is mainly caused by annealing and CMP. As shown in Fig. 4c, about 10 nm of silicon nitride film was removed by CMP each time. Annealing is the main reason

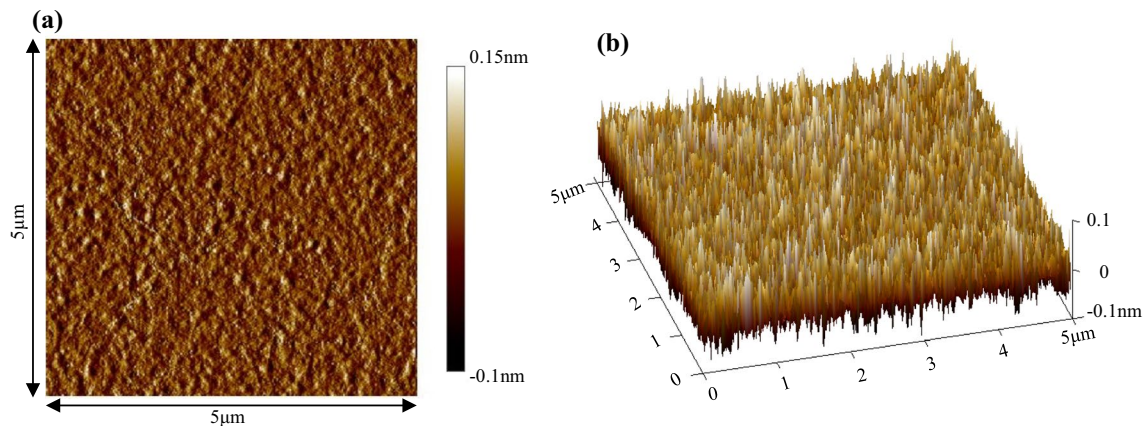


**Fig. 2** AFM images of surface of 400-nm-thick silicon nitride films (after CMP): (a) 2D and (b) 3D plots

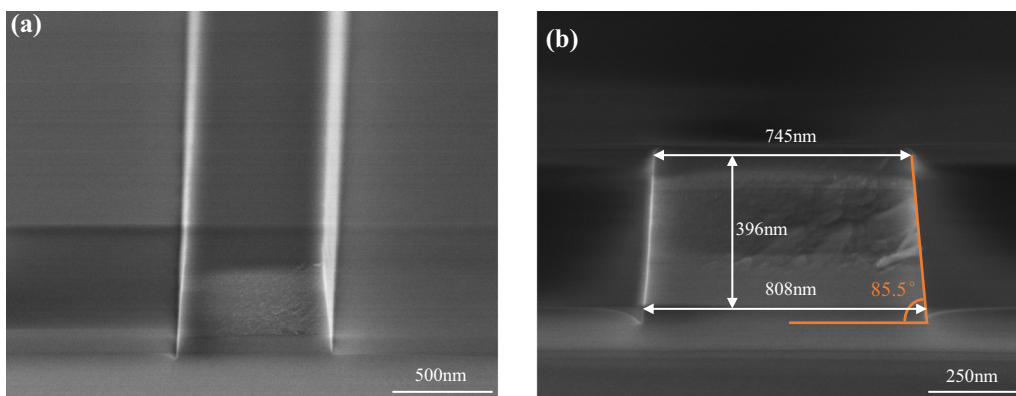


Fig. 3 SEM of 800-nm-width strip waveguide: (a) top view at 30°; (b) cross-section view

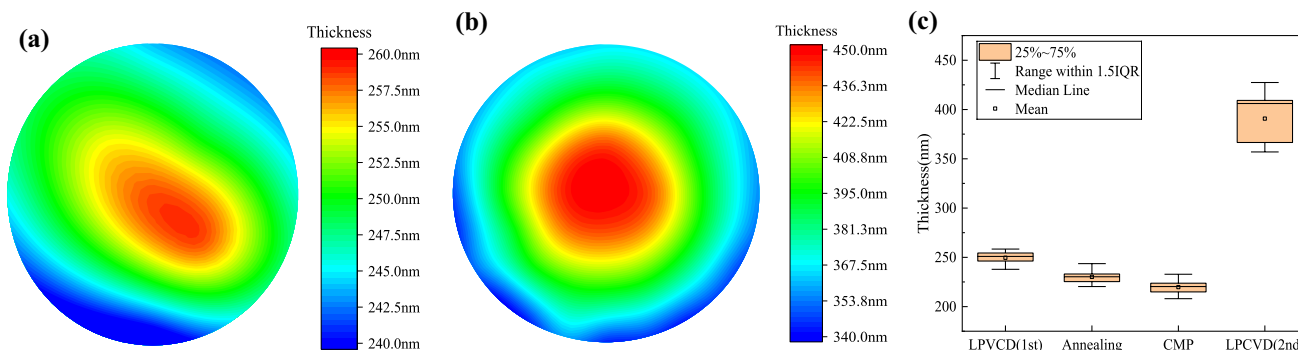


Fig. 4 The thickness of silicon nitride films: (a) representative map (after first deposition), (b) representative map (after second deposition), and (c) box plot of each process

leading to the reduction of thickness. The thickness of the films decreased from 249 nm to 231 nm after the first annealing. Because of the atomic rearrangement during annealing, film densification occurred and the thickness decreased. The thickness change due to film densification can be described by an exponential function with a time constant, which is considered to be the film relaxation time.<sup>20</sup> The relationship between the film thickness and annealing time can be described as follows:

$$h(t) = [h(0) - h(\infty)]e^{-\frac{t}{\tau}} + h(\infty), \tag{1}$$

where  $h(0)$  and  $h(\infty)$  denote the initial thickness and the thickness of the film after infinite annealing time, respectively.  $\tau$  is the time constant, having an empirical value of about 22 min at 1100°C.<sup>19</sup> Therefore, it can be calculated that each annealing will reduce the thickness of the silicon nitride film by about 7%, which is consistent with the experimental results.

### FTIR Analysis

Fourier-transform infrared (FTIR) spectroscopy is an important tool for characterizing silicon nitride films. It is generally used to obtain information about the bonding configuration and composition of films. The wavelengths of peaks in the FTIR spectrum reflect the chemical bonding structure in the molecule, which can be used to identify the composition of the film. FTIR measurements were carried out in the mid-infrared region from 400  $\text{cm}^{-1}$  to 4000  $\text{cm}^{-1}$  for the silicon nitride films by using a Thermo-Nicolet 6700 FTIR spectrometer (Fig. 5). Bands were observed at 470  $\text{cm}^{-1}$ , 840  $\text{cm}^{-1}$ , 1150  $\text{cm}^{-1}$ , 2180  $\text{cm}^{-1}$ , and 3350  $\text{cm}^{-1}$ , which correspond to Si–N symmetric stretching, Si–N asymmetric stretching, N–H wagging, Si–H stretching, and N–H stretching modes, respectively.<sup>21,22</sup> The signals for Si–H bonds at 2180  $\text{cm}^{-1}$  and N–H bonds at 3350  $\text{cm}^{-1}$  disappeared after annealing, indicating their breakage at high temperatures.

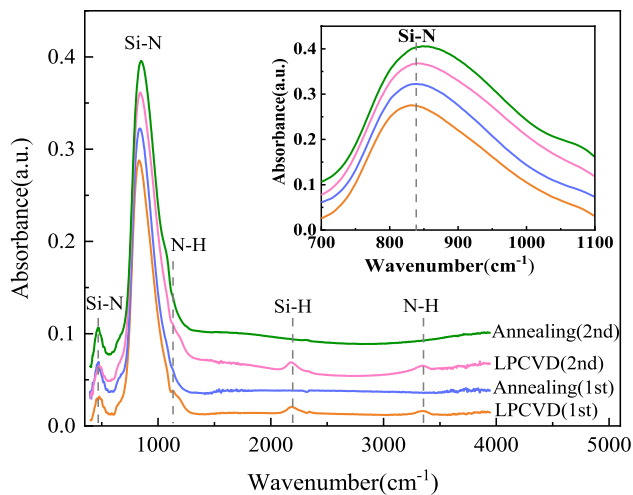


**Fig. 5** Absorbance spectra of silicon nitride films; Inset: absorption spectrum of Si–N asymmetric stretching peak

The inset of Fig. 5 shows that the intense absorption band corresponding to the Si–N asymmetric stretching mode was shifted from  $830\text{ cm}^{-1}$  to  $845\text{ cm}^{-1}$  after the two annealing processes, and the blue shift of the band positions indicates a decreasing Si content.<sup>23</sup> The Si–N asymmetric stretching mode can be assigned as transverse optical (TO) for light at normal incidence, and the TO band positions increase linearly with increasing Si/N ratio  $x$  according to the relation<sup>24</sup>

$$\nu_{\text{TO}}(x) = 21.4(x - 4/3) + \nu_{\text{TO}}(4/3), \quad (2)$$

where  $x$  is the N/Si ratio,  $\nu_{\text{TO}}(x)$  is the TO band position, and  $\nu_{\text{TO}}(4/3)$  is the TO band position for the stoichiometric condition, having a value of about  $840\text{ cm}^{-1}$ .<sup>25</sup> According to Eq. 2, it can be calculated that the silicon nitride films after two annealing processes were close to stoichiometric  $\text{Si}_3\text{N}_4$ .

### Residual Stress and Refractive Index

The level of residual stress is an important characteristic of silicon nitride film, being composed of thermal stress and intrinsic stress. The thermal stress is caused by the mismatch of thermal expansion coefficient between the film and substrate. The intrinsic stress is caused by lattice mismatch, crystallization, crystallite coalescence at grain boundaries, and phase transformations.<sup>26</sup> Tensile stress exceeding the film strength will cause cracks in the wafer. The silicon nitride films were deposited on the buried oxide layer via LPCVD in two steps, each followed by annealing, which can effectively overcome the problem of excessive stress.

The residual stress (measured by a Toho FLX-2320-S thin film stress machine) and the refractive index at a wavelength of 633 nm (measured by a Nanometrics Nanospec 9100) of the silicon nitride films after each step of the process are

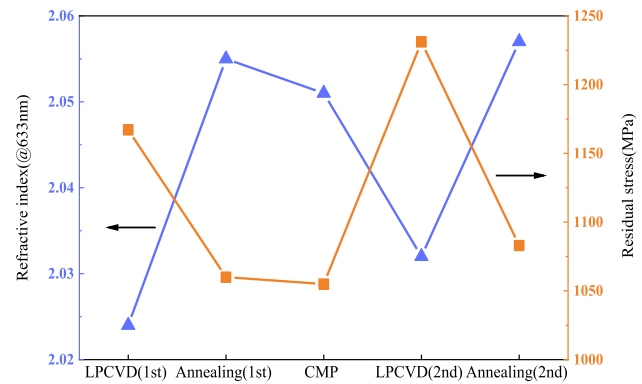


**Fig. 6** Residual stress and refractive index of silicon nitride films

shown in Fig. 6. The stress of the films decreased from about 1200 MPa to 1050 MPa after annealing. This is because, with the increase of temperature, the activation energy of nitrogen and silicon atoms in the films are increased, which causes the defects formed during the deposition process, such as vacancies, interstitials, and dislocations, to recombine or move to grain boundaries and disappear. As a result, the intrinsic stress of the silicon nitride films is reduced. In addition, annealing can release H atom in the films, and as the film becomes silicon rich, its refractive index increases.

## Optical Measurements

### Strip Waveguide

The strip waveguide is a fundamental device in silicon photonics. The performance of waveguides directly affects the entire photonic integration circuit, but also indicates the quality of silicon nitride films. The single-mode condition of a strip waveguide simulated by the finite-difference time-domain (FDTD) method is shown in Fig. 7a; the width of the single-mode waveguide was designed to be 800 nm. The cut-back method was used to measure the propagation loss for a wafer-level waveguide.<sup>27</sup> In this case, the propagation loss can be extracted by fitting a linear model to the measured optical transmission values (dB) as a function of length (cm), as the slope of the line corresponding to the best fit provides an estimate of the waveguide loss. This method is a powerful tool that removes the influence of factors such as coupling loss and bend loss.

A tunable laser was employed as the input light source, and a polarization controller was connected to the laser source to tune the input light to be transverse electric (TE) polarization. The laser source was coupled to the chip through a focusing grating coupler. The length of the waveguides was designed to be 4 cm, 6 cm, 10 cm, 20 cm, and 30 cm, respectively. As shown in Fig. 7b, c, the propagation loss of the 800-nm-wide waveguide was approximately 0.5

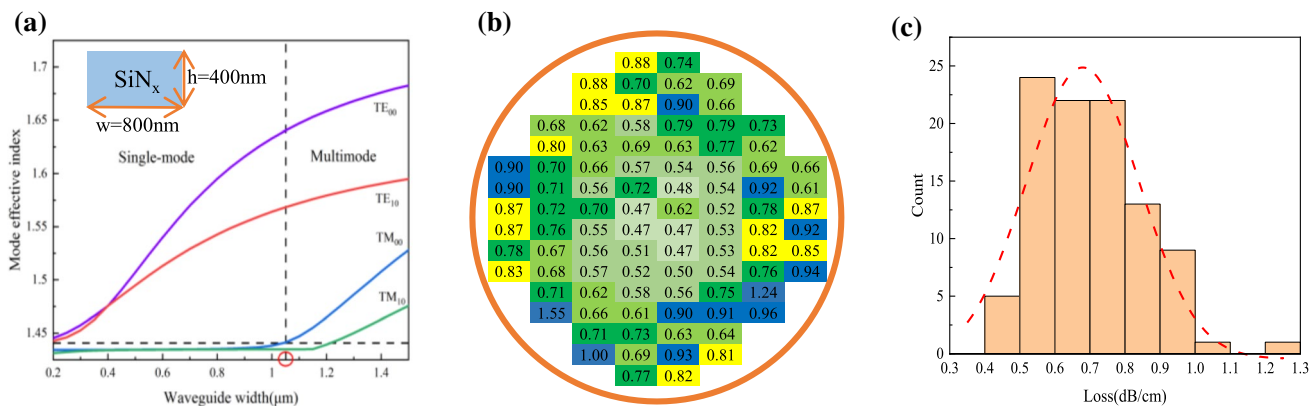


Fig. 7 Strip waveguide: (a) single-mode condition, (b) wafer-level loss measurements, and (c) histogram of propagation loss

Table I Summary of propagation losses (at 1550 nm) for silicon nitride waveguides deposited by LPCVD

Size of Wafer (mm)	Dimensions, Height × Width (nm × nm)	Propagation Loss (dB/cm)	Ref.
/	400 × 1000	1.3	28
/	400 × 1000	0.72	29
100	800 × 800	0.37	30
200	730 × 750	1.7	16
200	400 × 800	0.5–0.7	[Current work]

dB/cm to 0.7 dB/cm for the C-band, indicating that the silicon nitride films can satisfy the requirements for low-loss passive photonic devices. The loss was less than 0.5 dB/cm in the center of the wafer, but about 0.9 dB/cm at the edge of the wafer. This is because, at the edge of the wafer, the thickness of the silicon nitride films decreased and the confinement of the field was weakened, resulting in higher loss.

Furthermore, a comparison of the propagation losses at a wavelength of 1550 nm for the different silicon nitride

waveguides deposited by LPCVD is presented in Table I. Compared with other waveguides of the same thickness, the waveguide deposited in two steps showed lower propagation loss, and this process could be used on larger-size wafers.

### Waveguide Crossing

A waveguide crossing is a key device in optical communication networks and data centers, mainly being used to achieve crossing connections between multiwavelength networks.<sup>31</sup> Thus, achieving crossings with low loss and low crosstalk is very important for photonic integration. Figure 8a shows the optical power profile at a wavelength of 1550 nm passing through the crossing according to the 3D-FDTD simulation. The footprint of the crossing was 60 μm × 60 μm. A SEM image of the waveguide crossing is shown in Fig. 8b. The measured spectra shows that the insertion loss of waveguide crossing was approximately 0.15 dB, while the crosstalk was below -43 dB over the wavelength range from 1520 nm to 1600 nm.

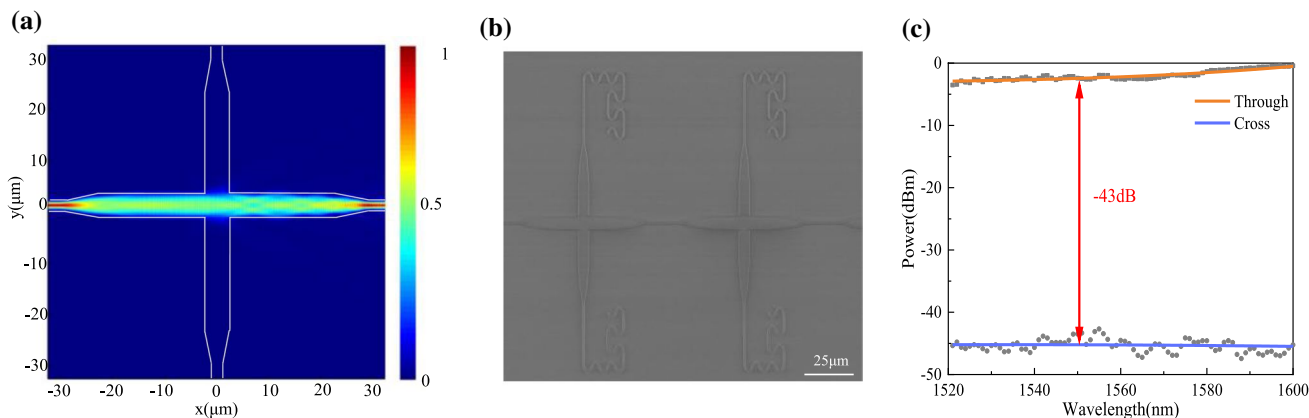
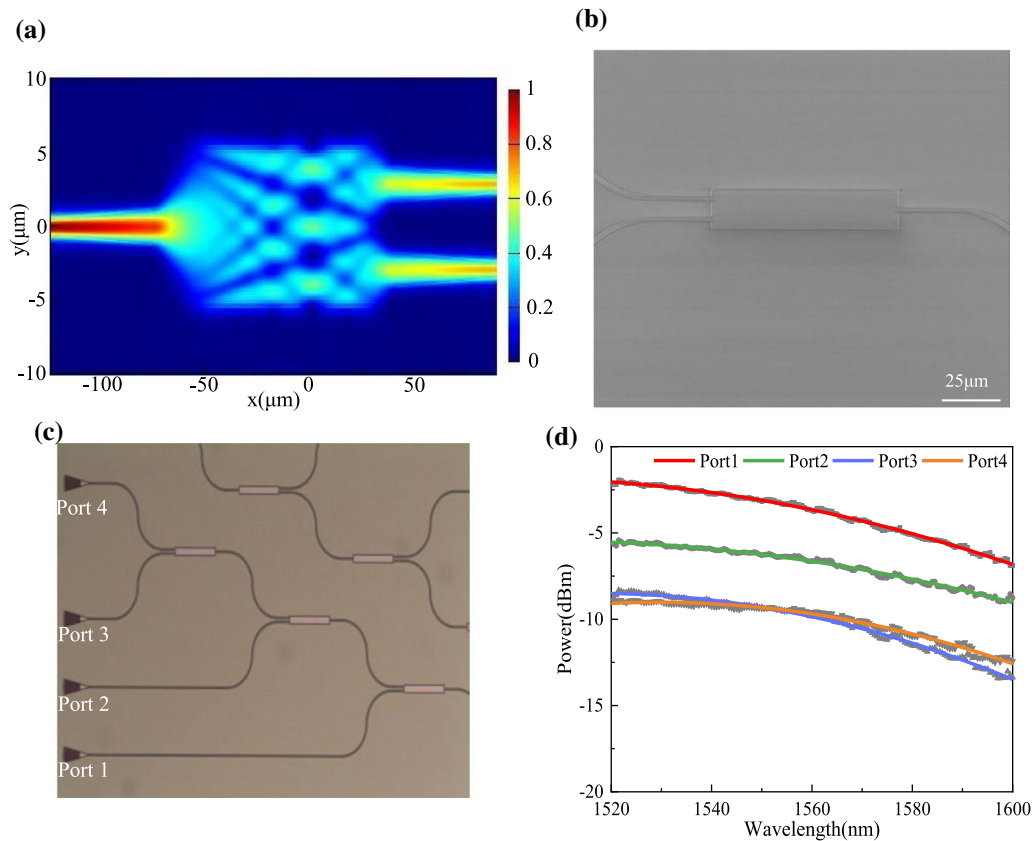


Fig. 8 Waveguide crossing: (a) 3D-FDTD simulated profile, (b) SEM, and (c) measured spectra



**Fig. 9** MMI: (a) 3D-FDTD simulated profile, (b) SEM, (c) test structure, and (d) measured spectra of four ports

## MMI

Multimode interference (MMI) offers the advantages of low insertion loss, large bandwidth, simple structure, and strong fault tolerance, being widely used in wavelength division multiplexing (WDM), optical switching, and other fields.<sup>32,33</sup> Figure 9a shows the optical power profile at a wavelength of 1550 nm passing through a  $1 \times 2$  MMI according to the 3D-FDTD simulation. The length of the MMI section ( $L_{\text{MMI}}$ ) was 81.5  $\mu\text{m}$ , and the width of the MMI section ( $W_{\text{MMI}}$ ) was 12  $\mu\text{m}$ . The SEM image is shown in Fig. 9b. The  $1 \times 2$  MMI, as the 3 dB splitter, has the cascade testing structure shown in Fig. 9c. It was measured that the insertion loss of MMI was lower than 0.3 dB while the nonuniformity was less than 10%.

## Conclusions

Crack-free 400-nm-thick silicon nitride films were successfully deposited by LPCVD using the 200-mm CMOS platform. LPCVD was applied in two steps to reduce the tensile stress in the silicon nitride films effectively. FTIR spectra showed that the silicon nitride films were close to

stoichiometric  $\text{Si}_3\text{N}_4$ , indicating that the films will have better optical performance. CMP was used to reduce the surface roughness after deposition and thus reduce the light scattering from the surface and grain boundaries. A strip waveguide with propagation loss as low as 0.5 dB/cm for the C-band was obtained using this process. In addition, other low-loss passive devices such as a waveguide crossing and MMI were demonstrated, promoting high-performance and large-scale silicon-based photonic integration.

**Acknowledgments** The whole process of silicon nitride films was based on the CMOS lines of Institute of Microelectronics, Chinese Academy of Sciences. The authors thank the staff of the IMECAS's CMOS lines. This work was supported by Beijing Municipal Natural Science Foundation (No. 4202079).

**Conflict of Interest** The authors declare that they have no conflicts of interest.

## References

1. W. Bogaerts, and L. Chrostowski, *Laser Photon. Rev.* 12, 1700237 (2018).
2. Y. Su, Y. Zhang, C. Qiu, X. Guo, and L. Sun, *Adv. Mater. Technol.* 5, 1901153 (2020).

3. H. Yu, J. Doyle, W. Lin, K. Nguyen, W. Liu, D. Gold, A. Dahal, C. Jan, R. Herrick, G. Ghiurcan, S. Hollingsworth, R. Romero, M. Favaro, L. Qiu, D. Zhu, and Y. Akulova, in *Optical Fiber Communication Conference*, W3E.4 (2019).
4. S.A. Miller, Y.C. Chang, C.T. Phare, C.S. Min, M. Zadka, S.P. Roberts, B. Stern, X. Ji, A. Mohanty, O.J. Gordillo, D. Dave, and M. Lipson, *Optica* 7, 3 (2020).
5. T.D. Bucio, C. Lacava, M. Clementi, J. Faneca, I. Skandalos, A. Baldycheva, M. Galli, K. Debnath, P. Petropoulos, F. Gardes, and I.E.E.E.J. Sel, *Top Quant. Electron.* 26, 1 (2020).
6. J.M. Fedeli, and S. Nicoletti, *Proc. IEEE* 106, 2302 (2018).
7. X. Qiang, Y. Wang, S. Xue, R. Ge, L. Chen, Y. Liu, A. Huang, X. Fu, P. Xu, T. Yi, M. Deng, J.B. Wang, J. Meinecke, J. Matthews, X. Cai, X. Yang, and J. Wu, *Sci. Adv.* 7, 8375 (2021).
8. A. Katumba, M. Freiburger, F. Laporte, A. Lugnan, S. Sackesyn, C. Ma, J. Dambre, P. Bienstman, and I.E.E.E.J. Sel, *Top Quant. Electron.* 24, 1 (2018).
9. T.D. Bucio, C. Lacava, M. Clementi, J. Faneca, I. Skandalos, A. Baldycheva, M. Galli, K. Debnath, P. Petropoulos, F. Gardes, and I.E.E.E.J. Sel, *Top Quant. Electron.* 26, 8200613 (2019).
10. J.C. Mikkelsen, W.D. Sacher, and J.K. Poon, *Opt. Express* 22, 3145 (2014).
11. D.J. Moss, R. Morandotti, A.L. Gaeta, and M. Lipson, *Nat. Photon.* 7, 597 (2013).
12. R. Baets, A.Z. Subramanian, S. Clemmen, B. Kuyken, P. Bienstman, N.L. Thomas, G. Roelkens, D.V. Thourhout, P. Helin, and S. Severi, In *Optical Fiber Communications Conference*, Th3J.1 (2016)
13. E. Bustarret, M. Bensouda, M.C. Habrard, and J.C. Bruyère, *Phys. Rev. B* 38, 8171 (1988).
14. Z. Yin, and F.W. Smith, *Phys. Rev. B* 42, 3666 (1990).
15. C.H. Henry, R.F. Kazarinov, H.J. Lee, K.J. Orlowsky, and L.E. Katz, *Appl. Opt.* 26, 2621 (1987).
16. E.H. Dirani, M. Casale, S. Kerdiles, C.C. Socquet, X. Letartre, C. Monat, and C. Sciancalepor, *IEEE Photon. Technol. Lett.* 30, 355 (2018).
17. Y. Chris, and P. John, *SILICON* 10, 2561 (2018).
18. X. Ji, F.A.S. Barbosa, and S.P. Roberts, *Optica* 4, 619 (2017).
19. W. Jiang, D. Xu, S. Yao, B. Xiong, and Y. Wang, *Mater. Sci. Semicond. Process.* 43, 222 (2016).
20. A.G. Noskov, E.B. Gorokhov, G.A. Sokolova, E.M. Trukhanov, and S.I. Stenin, *Thin Solid Films* 162, 129 (1988).
21. D.V. Tsu, G. Lucovsky, and M.J. Mantini, *Phys. Rev. B* 33, 7069 (1986).
22. S.K. Ghosh, and T.K. Hatwar, *Thin Solid Films* 166, 359 (1988).
23. M. Ippolito, and S. Meloni, *Phys. Rev. B* 83, 5209 (2011).
24. I. Guler, *Mater. Sci. Eng. B Adv.* 246, 21 (2019).
25. O. Debieu, R.P. Nalini, J. Cardin, X. Portier, J. Perrière, and F. Goubilleau, *Nanoscale Res. Lett.* 8, 31 (2013).
26. K.-S. Chen, in *MEMS/NEMS*, ed. by C. T. Leondes (Springer, Boston, 2006), p. 1252–1328
27. A. Peczek, C. Mai, G. Winzer, and L. Zimmermann, In *IEEE 33rd International Conference on Microelectronic Test Structures*, 19743952 (2020)
28. Y. Huang, J. Song, X. Luo, T.Y. Liow, and G.Q. Lo, *Opt. Express* 22, 21859 (2014).
29. H. Zhang, L. Chao, X. Tu, X. Luo, M. Yu, and G.Q. Lo, *Appl. Phys. A* 115, 79 (2014).
30. J.P. Epping, M. Hoekman, R. Mateman, A. Leinse, R.G. Heide- man, A. Van Rees, P.J.M. Van, C.J. Lee, and K.J. Boller, *Opt. Express* 23, 642 (2015).
31. S. Wu, X. Mu, L. Cheng, S. Mao, and H.Y. Fu, *Micromachines* 11, 326 (2020).
32. J. Mu, A.V. Sergio, M.A. Sefunc, Y. Yong, and M.G. Sonia, *J. Lightw. Technol.* 34, 3603 (2016).
33. F. Duan, K. Chen, D. Chen, and Y. Yu, *Opt. Lett.* 46, 234 (2020).

**Publisher's Note** Springer Nature remains neutral with regard to jurisdictional claims in published maps and institutional affiliations.